$- 1] \times 10^3$, where the standard, described in (*27*), is an ultrapure sample of $CaCO_3$.

12. P. Zhu and J. D. Macdougall, *Geochim. Cosmochim. Acta* **62**, 1691 (1998).
13. The procedures for the chemical separation and mass spectrometric analysis of calcium are modified from those described in Russell *et al.* (*37*) and Marshall and DePaolo (*38*) and are described by Skulan *et al.* (*27*). A mixed ^{42}Ca-^{48}Ca tracer is added to carbonate samples that have been dissolved in HCl or is added directly to seawater samples. With the seawater samples, the sample-tracer mixture is loaded onto a cation-exchange column packed with Dowex resin and eluted with HCl. Calcium is then loaded onto Ta filaments for mass spectrometric analysis on a VG Sector 54E modified to have one large bucket Faraday collector. Using three ratios, $^{42}Ca/^{40}Ca$, $^{44}Ca/^{40}Ca$, and $^{48}Ca/^{40}Ca$, we solve for three unknowns: the tracer/sample ratio, the mass discrimination, and the sample $^{44}Ca/^{40}Ca$ ratio. Solution of the equations is done iteratively.
14. C. H. Chen, D. J. DePaolo, C.-Y. Lan, *Earth Planet. Sci. Lett.* **143**, 125 (1996).
15. D. J. DePaolo and K. L. Finger, *Geol. Soc. Am. Bull.* **103**, 112 (1991).
16. F. M. Richter, D. B. Rowley, D. J. DePaolo, *Earth Planet Sci. Lett.* **109**, 11 (1992).
17. D. A. Hodell and F. Woodruff, *Paleoceanography* **9**, 405 (1994).
18. J. S. Oslick, K. G. Miller, M. D. Feigenson, J. D. Wright, *Paleoceanography* **9**, 427 (1994).
19. K. G. Miller, R. G. Fairbanks, G. S. Mountain, *Paleoceanography* **2**, 1 (1987).
20. J. M. Gieskes and J. R. Lawrence, *Geochim. Cosmochim. Acta* **45**, 1687 (1981).
21. H. Elderfield and A. Schultz, *Annu. Rev. Earth Planet. Sci.* **24**, 191 (1996).
22. The dominant input of Ca^{2+} to the ocean comes from rivers, with 1.2×10^{13} to 1.5×10^{13} mol $year^{-1}$ being the current estimate (*39*, *40*). The major output of Ca^{2+} occurs as the deposition of carbonate sediments on the seafloor, presently estimated at 2.9×10^{13} mol $year^{-1}$ (*41*).
23. M. G. Erskian and J. H. Lipps, *J. Foraminiferal Res.* **17**, 240 (1987).
24. *Emiliania huxleyi* isolate CCMP 1742 (Provasoli-Guillard National Center for Culture of Marine Phytoplankton) was grown under cool white lights, on a 14-10 hour light-dark cycle at 16°C in f/2-Si media (*42*).
25. J. Skulan and D. J. DePaolo, *Proc. Natl. Acad. Sci. U.S.A.* **96**, 13709 (1999).
26. Examples of wider variability (fractionations of −0.47 and −0.88‰ relative to seawater) are provided by tests of the tropical foraminifera, *Alveolinella quoyi* and *Marginopora vertebralis* (*23*). Both *A. quoyi* and *M. vertebralis* are unusually large foraminifera (with diameters up to 12 and 30 mm, respectively) and harbor photosynthetic symbionts (*43*, *44*). Both of these features may affect Ca^{2+} uptake and mineralization rates and thus potentially alter Ca^{2+} isotopic fractionation.
27. J. Skulan, D. J. DePaolo, T. L. Owens, *Geochim. Cosmochim. Acta* **61**, 2505 (1997).
28. Values for the Ca^{2+} isotopic composition of rivers reported by Zhu and MacDougall (*12*) were normalized to our standard, purified $CaCO_3$ (*27*) with seawater (the only material common to both studies) as an anchor point. The isotopic value of the rivers relative to the $CaCO_3$ standard ($\delta^{44}Ca_{CCStd}$) are equal to the isotopic difference between the rivers and seawater measured with the old standard minus the difference between the $CaCO_3$ standard and seawater relative to $CaCO_3$: $\delta^{44}Ca_{riverCCstd} = (\delta^{44}Ca_{riveroldstd} - \delta^{44}Ca_{SWoldstd}) - (\delta^{44}Ca_{CCstd} - \delta^{44}Ca_{SWCCstd})$ or $\delta^{44}Ca_{CCstd} = (\delta^{44}Ca_{riveroldstd} - 0‰) - (0‰ - 0.9‰)$.
29. The silicate weathering flux to the oceans may have a $\delta^{44}Ca$ that is lower than the average $\delta^{44}Ca$ of igneous rocks if there is fractionation associated with weathering. If so, there is an additional reservoir with relatively high $\delta^{44}Ca$ composed of silicate weathering residues. Hence, clay-rich sediments and some soils may have significantly elevated $\delta^{44}Ca$ values.
30. The modern system is not at steady-state owing to effects related to the last deglaciation (*45*). However, because the duration of the imbalance is so short (10,000 years) relative to the residence time of Ca^{2+} in seawater, there is no observable $\delta^{44}Ca$ effect.
31. R. B. Sorkhabi and E. Stump, *Geol. Soc. Am. Today* **3**, 85 (1993).
32. T. M. Harrison, P. Copeland, W. S. F. Kidd, A. Yin, *Science* **255**, 1663 (1992).
33. P. Copeland, T. M. Harrison, W. S. F. Kidd, R. Xu, Y. Zhang, *Earth Planet. Sci. Lett.* **86**, 240 (1987).
34. S. Guillot, K. Hodges, P. LeFort, A. Pecher, *Geology* **22**, 559 (1994).
35. The solubility product constant for calcite can be written in the form: $K_{sp} = [Ca^{2+}][HCO_3^-]^2/P_{CO_2}$. An increase in $[Ca^{2+}]$ will accompany an increase in P_{CO_2} in the absence of effects from other ions in solution (*46*). If pH is buffered, an increase in $[Ca^{2+}]$ would be compensated by a decrease in P_{CO_2}. To fully constrain P_{CO_2} requires an independent measure of pH, such as the boron isotopic composition of foraminifera (*47*, *48*). The temperature dependence of K_{sp}, the concentrations of other ions in seawater, and differences between the surface and deep ocean also come into play.
36. M. Pagani, K. H. Freeman, M. A. Arthur, *Science* **285**, 876 (1999).
37. W. A. Russell, D. A. Papanastassiou, T. A. Tombrello, *Geochim. Cosmochim. Acta* **42**, 1075 (1978).
38. B. D. Marshall and D. J. DePaolo, *Geochim. Cosmochim. Acta* **46**, 2537 (1982).
39. M. Meybeck, *Rev. Geol. Dyn. Geogr. Phys.* **21**, 215 (1979).
40. J. D. Milliman, *Global Biogeochem. Cycles* **7**, 927 (1993).
41. B. N. Opdyke and B. H. Wilkinson, *Paleoceanography* **3**, 685 (1988).
42. R. R. L. Guillard, in *Culture of Marine Invertebrate Animals*, W. L. Smith and M. H. Chanley, Eds. (Plenum, New York, 1975), pp. 26–60.
43. J. H. Lipps and K. P. Severin, *Sci. New Guinea* **11**, 126 (1984/85).
44. Y. Song, R. G. Black, J. H. Lipps, *Paleobiology* **20**, 14 (1994).
45. E. K. Berner and R. A. Berner, *Global Environment: Water, Air, and Geochemical Cycles* (Prentice-Hall, Upper Saddle River, NJ, 1996).
46. J. J. Drever, *The Geochemistry of Natural Waters* (Prentice-Hall, Englewood Cliffs, NJ, 1982).
47. P. N. Pearson and M. R. Palmer, *Science* **284**, 1824 (1999).
48. A. J. Spivack, C. F. You, H. J. Smith, *Nature* **363**, 149 (1993).

49. We thank T. Owens, B. L. Ingram, H. Tolliver, E. B. Roark, J. Skulan, J. Lipps, A. Lessen, M. Hendricks, D. Schrag, C. M. Preston, K. Wetmore, P. N. Froelich, the BATS crew, M. H. Garcia, and D. Penry for samples, advice, and assistance, and two anonymous reviewers for helpful comments. Supported by NSF grants EAR9526997 and EAR9909639 (D.J.D.) and by a University of California, Berkeley, Chancellor's Postdoctoral Fellowship (C.L.D.).

5 April 2000; accepted 20 June 2000

Earthquake Potential Along the Northern Hayward Fault, California

Roland Bürgmann,[1]* D. Schmidt,[1] R. M. Nadeau,[1] M. d'Alessio,[1] E. Fielding,[2] D. Manaker,[3] T. V. McEvilly,[1] M. H. Murray[1]

The Hayward fault slips in large earthquakes and by aseismic creep observed along its surface trace. Dislocation models of the surface deformation adjacent to the Hayward fault measured with the global positioning system and interferometric synthetic aperture radar favor creep at ~7 millimeters per year to the bottom of the seismogenic zone along a ~20-kilometer-long northern fault segment. Microearthquakes with the same waveform repeatedly occur at 4- to 10-kilometer depths and indicate deep creep at 5 to 7 millimeters per year. The difference between current creep rates and the long-term slip rate of ~10 millimeters per year can be reconciled in a mechanical model of a freely slipping northern Hayward fault adjacent to the locked 1868 earthquake rupture, which broke the southern 40 to 50 kilometers of the fault. The potential for a major independent earthquake of the northern Hayward fault might be less than previously thought.

On 21 October 1868, the only known historic major earthquake [magnitude (M) ≈ 7] on the Hayward fault ruptured the southern fault segment over a distance of 40 to 50 km from Fremont to Berkeley (Fig. 1A) (*1*). Investigations of paleoseismic (*2*) and historic (*3*) data suggest that the most recent earthquake north of the 1868 rupture occurred between 1640 and 1776. Long-term slip rate estimates of ~10 mm/year suggest that 2.2 to 3.6 m of seismic slip potential have accumulated since the most recent event on the northern Hayward fault (*4*, *5*). Thus, the Hayward–Rodgers Creek fault zone is commonly assigned the highest earthquake probability of any fault in the San Francisco Bay area (*6*). However, estimates of elastic strain to be released in future events are complicated by the occurrence of aseis-

[1]Department of Earth and Planetary Science and Berkeley Seismological Laboratory, 307 McCone Hall, University of California, Berkeley, Berkeley, CA 94720, USA. [2]Mail Stop 300-233, Jet Propulsion Laboratory, California Institute of Technology, 4800 Oak Grove Drive, Pasadena, CA 91109, USA. [3]Department of Geology, University of California, Davis, Davis, CA 95616, USA.

*To whom correspondence should be addressed. E-mail: burgmann@seismo.berkeley.edu

mic creep (*4*, *7*) along the surface trace of the Hayward fault whose depth extent is not known.

The northern Hayward fault exhibits steady surface creep of 5 to 6 mm/year (Fig. 2B) (*4*, *7*). Two-dimensional fault modeling indicated that with a 5 mm/year surface creep rate the aseismic slip reaches only to ~5-km depth and does little to reduce the earthquake hazard on the fault (*5*). Previously available geodetic data did not allow for the discrimination of models of the Hayward fault creeping to shallow (~5 km) depth or to the bottom of the seismogenic zone (~12 km) (*4*, *8*).

Geodetic measurements of surface displacements surrounding a fault can be used to determine subsurface slip rates on dislocations in an elastic half-space model (*9*, *10*). However, precisely surveyed sites near the Hayward fault are spaced more than 10 km apart, and it is therefore difficult to determine a reliable slip estimate from existing point measurements alone. Space-based interferometric synthetic aperture radar (InSAR) can map ground deformation at tens-of-meter spatial resolution with subcentimeter precision but only measures displacements along the look direction of the radar (*11*). Thus, to improve constraints on the rate and extent of aseismic Hayward fault slip, we integrated surface creep rates established over several decades (Fig. 2B), global positioning system (GPS) measurements from 1993 to 1999 (Fig. 1A), and InSAR measured range changes between 1992 and 1997 (Fig. 1). We also considered subsurface creep rates estimated from identical repeating microearthquakes on the fault that occurred from 1984 to 1999 (Fig. 2).

Surface creep rates are constrained by repeated surveys of alignment arrays across the fault (*7*), offsets of cultural features (*4*), and creepmeter measurements (*12*). GPS station velocities were computed from yearly campaign-mode measurements, as well as from monthly solutions of continuously operating receivers of the BARD (Bay Area regional deformation) network (*13*). The GPS data show the distribution of 35.6 ± 2.5 mm/year of right-lateral shear across the 107-km-wide network spanning the San Andreas fault system, with a localized velocity step near the northern Hayward fault (Fig. 1). We used SAR data collected by the European Space Agency's ERS spacecraft in 1992 and 1997 (*14*) to produce two ~5-year interferograms (*15*) (Fig. 1). We used filtered, unwrapped, and subsampled range-change-rate data (*16*) to determine the rate and depth extent of creep on the northern Hayward fault (Figs. 3 and 4).

To evaluate possible contributions of vertical fault offsets, we examined an interferogram taken from the ascending orbit of the ERS spacecraft, which traverses the region toward N13.9°W, at an angle of 28° from the descending-orbit track and only 20° off the Hayward fault strike. The interferogram of the ascending images showed no measurable discontinuity across the northern Hayward fault (Fig. 3). Because the ascending-orbit data are relatively insensitive to fault-parallel motion but equally sensitive to potential vertical fault offsets as the descending-orbit data, we can rule out substantial contributions of vertical fault slip to the descending-orbit offsets that could have biased our results (*17*). As longer wavelength atmospheric-delay artifacts affect the ascending interferogram, we did not include these data in our modeling.

We used rectangular dislocations in an elastic half-space model (*18*) and assumed that a model of uniform slip from the surface to some depth adequately characterizes creep along the northern 30 km of the Hayward fault. Regional interseismic strain accumulation across the San Andreas fault system is represented by strike slip on buried dislocations from 12 to 3000 km below the San Andreas, Hayward–Rodgers Creek, Calaveras, and Greenville fault zones. The regional fault slip rates were primarily determined by the GPS data (*19*), whereas the InSAR data constrained the slip rate and upper locking depth of the creeping northern Hayward fault. The two independent 1992–97 interferograms favored creep of ~7 mm/year (Fig. 4B) to depths of >6 km, with misfits decreasing as

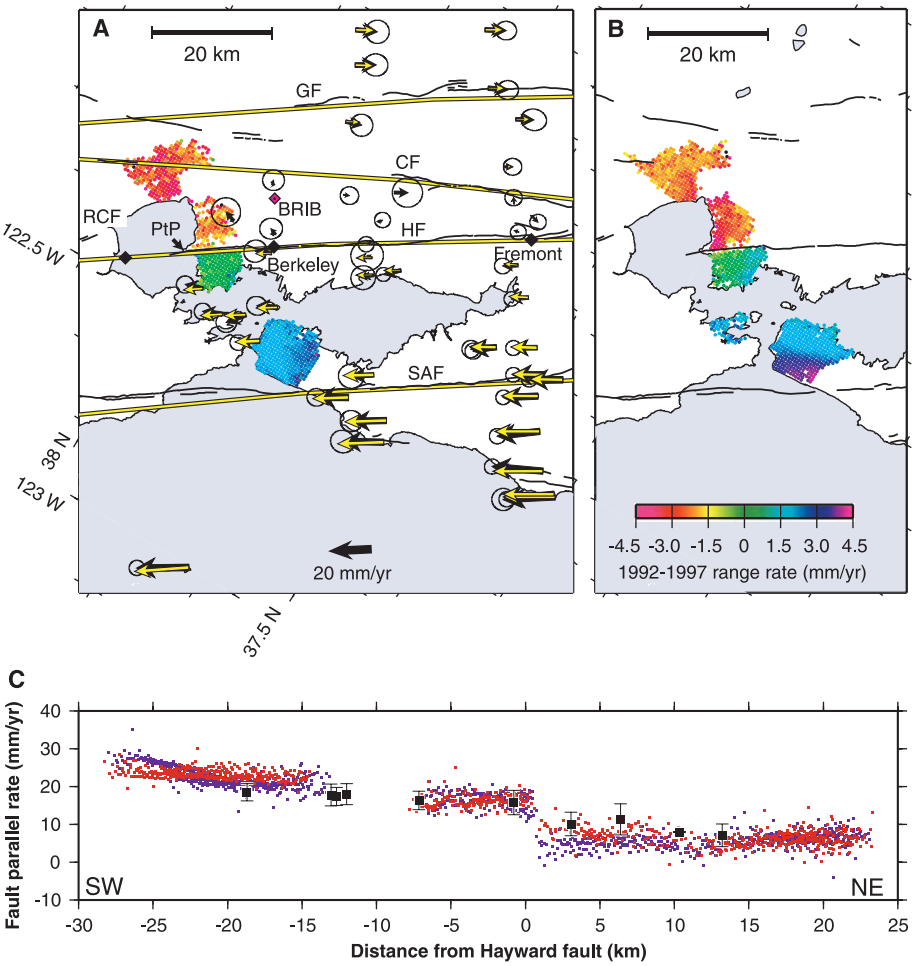

Fig. 1. (**A**) Fault map of San Francisco Bay area with horizontal GPS site velocities relative to station BRIB (black arrows) and their 95% confidence ellipses (PtP, Point Pinole; GF, Greenville fault; CF, Calaveras fault; RCF, Rogers Creek fault; HF, Hayward fault; and SAF, San Andreas fault). The map is drawn in an oblique Mercator projection about the angular velocity pole of Pacific plate to Sierra Nevada–Great Valley block motion (*26*). Also shown are predicted velocities (yellow arrows) from the six-dislocation model used to represent interseismic strain accumulation across the Bay area. Yellow-filled lines follow the dislocation planes; the end points of the two shallow Hayward fault segments are shown as black diamonds. The line-of-sight range change rates determined from the 10 June 1992 to 6 September 1997 interferogram are shown along a transect across the northern Hayward fault [see color bar in (B) for scale]. (**B**) 23 September 1992 to 2 August 1997 interferogram. (**C**) Profile of GPS velocities within 10 km of the InSAR transect (error bars are $\pm 1\sigma$). The InSAR-derived displacement rates along the transects in (A) and (B) are shown as blue (10 June 1992 to 6 September 1997) and red (23 September 1992 to 2 August 1997) dots. We assume that the line-of-sight changes are due to Hayward fault–parallel (N35°W) motions. The discrepancy between the two interferograms at the southwest end of the transect may be due to an atmospheric disturbance, such as fog, in the 23 September 1992 to 2 August 1997 image pair.

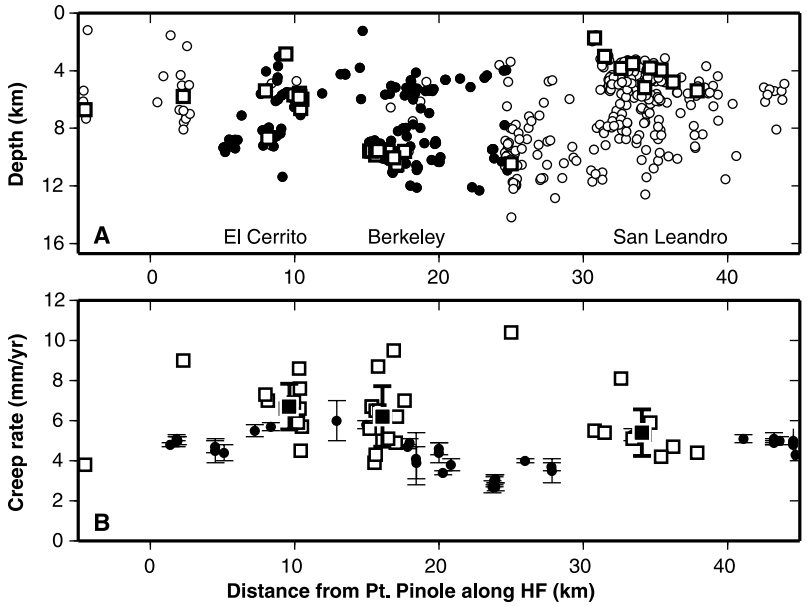

Fig. 2. (**A**) Depth section of microseismicity along the northern 50 km of the Hayward fault. Along-fault distances are in km from Point Pinole (Fig. 1). Events from within ±1.5-km distance of the fault are projected onto a N35°W-striking plane (1984–99 NCSN catalog locations shown as open circles). Along a 20-km-long segment of the fault, we show the precisely relocated events of Waldhauser *et al*. (*27*) as solid circles. Open squares indicate the locations of identically repeating event sequences used to compute subsurface creep rates. (**B**) Surface creep rates along northern Hayward fault (solid circles with ±1σ error bars) (*7*). Open squares indicate creep rates computed from the individual repeating-earthquake sequences (with an estimated standard deviation of ± 2.5 mm/year). Average creep rate estimates and their ±1σ data scatter are shown as filled squares for the three sequence clusters.

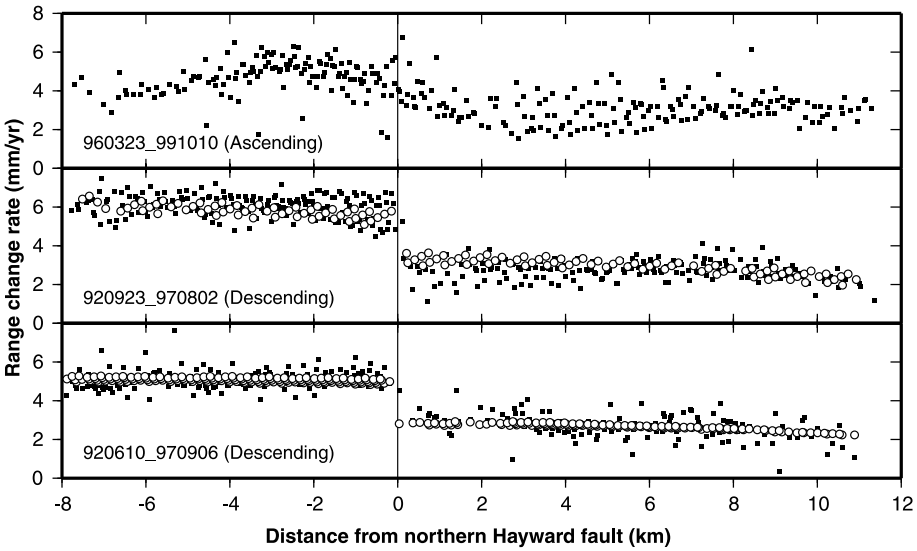

Fig. 3. Profiles of InSAR range change rates (black squares) from two descending- and one ascending-orbit image pairs. The ascending-orbit interferogram (top) does not reveal a discrete offset at the Hayward fault. In our model inversions, we used the descending-orbit InSAR data from within ±12 km of the fault with 293 and 342 data points from the 10 June 1992 to 6 September 1997 (bottom) and 23 September 1992 to 2 August 1997 (middle) interferograms, respectively. Also shown are predicted range change rates (open circles) from the two best-fitting models, which suggest creep rates of 7.1 and 7.3 mm/year to 12-km depth.

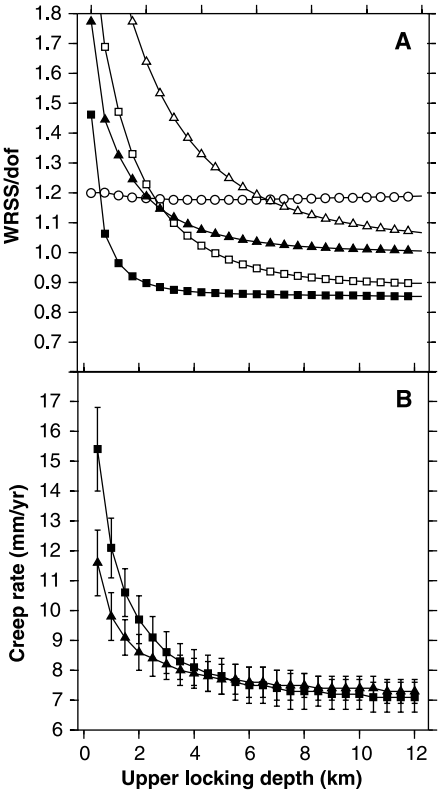

Fig. 4. (**A**) Misfit versus depth of creeping model Hayward fault. Misfit is the normalized weighted residual sum of squares, $WRSS/(N - P) = [(d_{obs} - d_{mod})^T \times cov^{-1} \times (d_{obs} - d_{mod})]/(N - P)$, where d_{obs} and d_{mod} are the observed and modeled data, cov is the data covariance matrix, N is the number of data, and P is the number of free model parameters (six fault slip rates and an offset and two orbital tilt parameters for the InSAR data). The full GPS data covariance matrix is included, whereas InSAR data are modeled as uncorrelated with 0.6 mm/year standard deviations. Circles are GPS misfits, squares are misfits of 10 June 1992 to 6 September 1997 interferogram, and triangles are for 23 September 1992 to 2 August 1997 interferogram. Open symbols are for models in which the secular deep slip rates are fixed to the best-fit rates from the GPS data and northern Hayward fault creep is held to 6 mm/year. Solid symbols indicate models in which all slip rates are solved for in-joint inversions of GPS and InSAR data. (**B**) Best-fitting creep rates on the northern Hayward fault determined from joint inversion of GPS and InSAR data as a function of upper locking depth. Squares and triangles denote interferograms as in (A).

the modeled dislocation approached the bottom (12 km) of the seismogenic zone (Fig. 4A). Although misfits were not significantly different for models with 5- to 12-km upper locking depth in the free inversion (solid symbols in Fig. 4A), the deeper models required lower creep rates (7.1 and 7.3 mm/year, Fig. 4B) that were more consistent with field-measured rates.

We interpret identical microearthquakes as small patches that repeatedly break in stick-slip events and are surrounded by the otherwise aseismically slipping fault (*20*, *21*). We identified 37 repeating sequences (comprising 83 earthquakes) from the Northern California Seismic Network (NCSN) earthquake catalog along a 50-km-long portion of the fault (Fig. 2A). Events in each sequence recurred two to three times and were used to estimate the distribution of subsurface fault creep rates (Fig. 2B) (*22*). Most of the repeat-

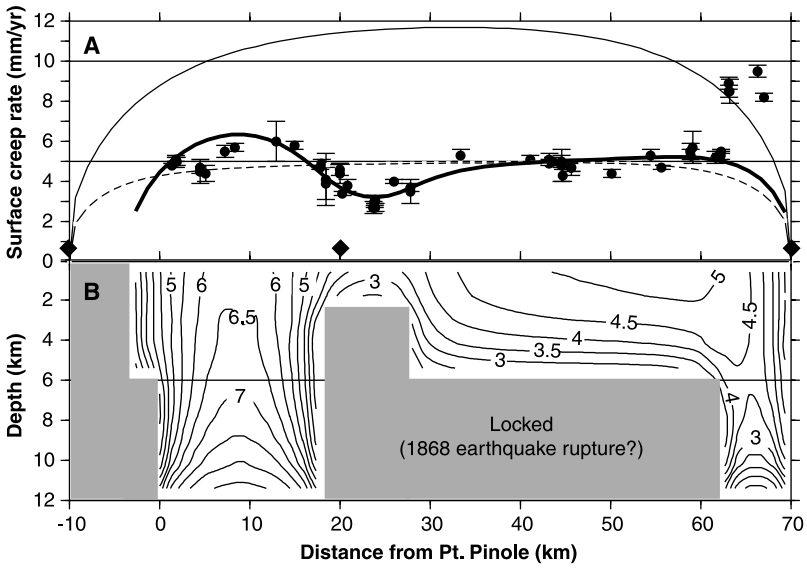

Fig. 5. (**A**) Surface creep rates predicted by models of a freely slipping Hayward fault loaded by secular slip below 12 km along the San Andreas (22.5 mm/year), Hayward (10 mm/year), and Calaveras (6 mm/year) faults. Creep data are solid circles with 1σ error bars (*8*). Diamond symbols correspond to those in Fig. 1A. Models shown are slip to 12 km along full length (thin solid line), locking from 6- to 12-km depth (dashed line), and locking along the southern Hayward fault only (bold solid line), which approximates the observed pattern. (**B**) Distribution of locked patches used in the model with a freely slipping northern Hayward fault segment. Subsurface model creep rates are contoured in millimeters per year.

ing events occur in three major clusters, whose average slip rates are 6.7 ± 1.1 mm/year (1 standard deviation) at 5.7-km depth (from 10 sequences), 6.2 ± 1.5 mm/year at 9.8-km depth (from 15 sequences), and 5.4 ± 1.2 mm/year at 3.9-km depth (from nine sequences) (Fig. 2B). The slip estimates from repeating earthquakes suggest subsurface creep at rates and depths consistent with those inferred from the surface deformation.

The primary argument for locking below 5-km depth along the entire Hayward fault is based on the observation of surface creep rates less than the long-term fault slip rates (*5*). To evaluate if the observed distribution of surface creep rates is consistent with a Hayward fault that is freely slipping north of the 1868 earthquake rupture, we used a boundary element model (*23*, *24*). This analysis expands previous studies (*5*) to address the three-dimensional geometry of the problem (*25*). Buried dislocations below 12-km depth along the San Andreas, Hayward, and Calaveras faults load the Hayward fault (Fig. 5). Creeping portions of the fault are modeled as shear-stress free patches allowing the determination of the resultant fault slip distribution. If the entire Hayward fault were freely creeping from the surface to 6-km depth, the surface creep rate along the fault would follow a smooth distribution with slip of up to 5 mm/year (dashed line in Fig. 5A). A model in which elastic strain accumulates about a locked segment along the southern Hayward fault (that might represent the ~40-km-long portion of the fault that broke in the 1868 rupture) and no locking occurs along a 20-km-long segment of the northern Hayward fault predicts the surface creep rates (bold line in Fig. 5A). Independent of the geodetic inversions and seismic data, the distribution of surface creep rates is consistent with a freely creeping northern fault segment. The portions of the fault that creep at rates less than the long-term slip rate are expected to catch up during and in the aftermath of 1868-type southern Hayward fault earthquakes and earthquakes on the Rodgers Creek fault to the north. This suggests that the northern segment of the Hayward fault should not be considered as an independent source region of large earthquakes.

References and Notes

1. E. Yu and P. Segall, *J. Geophys. Res.* **101**, 16101 (1996).
2. J. J. Lienkaemper *et al.*, *U.S. Geol. Surv. Open File Rep.* **99-318**, 1 (1999).
3. T. R. Toppozada and G. Borchardt, *Bull. Seismol. Soc. Am.* **88**, 140 (1998).
4. J. J. Lienkaemper, G. Borchardt, M. Lisowski, *J. Geophys. Res.* **96**, 18261 (1991).
5. J. C. Savage and M. Lisowski, *J. Geophys. Res.* **98**, 787 (1993).
6. Working Group on California Earthquake Probabilities, *U.S. Geol. Surv. Open File Rep.* **99-517** (1999).
7. J. J. Lienkaemper, J. S. Galehouse, R. W. Simpson, *Science* **276**, 2014 (1997).
8. W. H. Prescott and M. Lisawski, *Tectonophysics* **97**, 41 (1983).
9. R. Harris and P. Segall, *J. Geophys. Res.* **92**, 7945 (1987).
10. M. V. Matthews and P. Segall, *J. Geophys. Res.* **98**, 12153 (1993).
11. R. Bürgmann, P. A. Rosen, E. J. Fielding, *Annu. Rev. Earth Planet. Sci.* **28**, 169 (2000).
12. Data from a creepmeter at Pt. Pinole show a creep rate of 4.8 mm/year across a width of 15 to 23 m (R. Bilham, unpublished data).
13. Campaign GPS data from 1993 to 1999 were collected by the U.S. Geological Survey, Stanford University, and the University of California, Berkeley. The campaign data were processed with the Bernese 4.0 GPS processing software, and the BARD continuous data were processed with the GAMIT GPS processing software.
14. We selected the two image pairs with the longest temporal baselines and shortest orbit baselines that were collected during the summer to minimize tropospheric and land subsidence artifacts. Data are from descending ERS track 70, frames 2835 and 2853. The first pair includes scenes from 10 June 1992 to 6 September 1997 with an orbit baseline B_{perp} = 24 m, and the second image pair spans 23 September 1992 to 8 August 1997 with a B_{perp} = 54 m. To test for vertical fault offsets, we used an ascending-orbit (track 478, frame 747) image pair collected on 23 March 1996 and 10 October 1999 with a B_{perp} = 12 m.
15. We used InSAR data analysis software developed at the Jet Propulsion Laboratory to process the interferograms. Surface displacement rates are computed from the interferograms by unwrapping angular phase delays and converting the phase delay into line-of-sight range change rates. The ERS descending-orbit track trends S13.9°W with the radar looking westward at a 23° off-vertical look angle. Surface displacements and resulting range change are related as $\Delta\rho = \Delta\vec{d} \cdot \vec{e}$, where $\Delta\rho$ and $\Delta\vec{d}$ are the range change and surface displacement vectors, respectively, and $\vec{e}$ is the unit vector in the range direction (*11*). In the urban areas, the correlation between the SAR image pairs is high [with a coherence (*11*) of 0.25 to 0.7], whereas in the densely vegetated and steeply sloping areas, the image coherence is low (<0.2) so that the phase values are basically pure noise and were not used in the analysis. Topographic contributions to the apparent range changes were removed with a 30-m resolution U.S. Geological Survey digital elevation model. We removed a linear displacement gradient of 3.7×10^{-07} year^{-1} across the San Andreas fault system, which is well constrained by the GPS velocities, from the InSAR range change data before flattening (removal of orbital ramp during processing). This interseismic deformation ramp was added back into the interferogram during the final processing steps [G. Peltzer, F. Crampé, S. Hensley, *Eos Trans. AGU* **79**, 33 (1998)].
16. Data were filtered with a weighted power spectrum technique. Interferograms were processed with 8 range and 40 azimuth looks and subsampled with a nearest neighbor technique. Isolated patches of coherent phase were connected by manually specifying the integer wavelength offset between patches.
17. In the ascending-orbit data, 1 mm/year of right-lateral strike slip along the Hayward fault would result in −0.11 mm/year of range change (versus 0.28 mm/year for the descending-orbit geometry), whereas 1 mm/year of vertical offset would produce a 0.95 mm/year range change rate.
18. Y. Okada, *Bull. Seismol. Soc. Am.* **75**, 1135 (1985).
19. Best-fitting fault slip rates determined from the GPS data shown in Fig. 1A are 22.7 ± 1.7 mm/year below the San Andreas, 9.9 ± 2.5 mm/year below the Hayward–Rodgers Creek, 17.1 ± 5.1 mm/year below the Calaveras–Green Valley, and 2.5 ± 3.9 mm/year below the Greenville fault zones. The GPS-derived creep rates on the Hayward fault from the surface to 5-km depth are 7.4 ± 4.3 mm/year for the northern and 3.9 ± 1.7 mm/year for the southern segment. The model misfit $WRSS/(N - P)$ (Fig. 4) for this model is 1.13, indicating that the model provides a good fit to the data.
20. R. M. Nadeau and T. V. McEvilly, *Science* **285**, 718 (1999).
21. R. M. Nadeau and L. R. Johnson, *Bull. Seismol. Soc. Am.* **88**, 790 (1998).
22. We analyzed the available 1984–99 waveform data and used an empirical scaling equation relating average slip per event to its moment derived for Parkfield, CA (*21*), to estimate Hayward fault creep rates (*20*). We reestimated the empirical parameters using more data (1495 Parkfield events in 268 sequences) and using microearthquakes only ($-0.5 \leq M_w \leq 3.0$). This was done to eliminate a small size bias introduced by the assump-

tion of a greater loading rate of 33 mm/year for the Parkfield $M = 6$ sequence (*21*). The resulting relation is $v = 10^{(0.105M_w+0.45)}/T_{av}$, where v is in cm/year, T_{av} is the average recurrence interval for the sequence in years, and M_w is the moment magnitude. At a lower magnitude threshold of $M_w = 1.15$, we would not expect repeaters if slip rates were less than 3 mm/year for the 16-year period.

23. A. L. Thomas, thesis, Stanford University, Stanford, CA (1993).
24. R. Bürgmann, E. Fielding, J. Sukhatme, *Geology* **26**, 559 (1998).
25. R. Simpson (unpublished data) independently developed similar three-dimensional models of a frictionless Hayward fault, concluding that surface creep rates do not require a locked northern fault segment.
26. D. F. Argus and R. G. Gordon, *Geology* **19**, 1085 (1991).
27. F. Waldhauser, W. L. Ellsworth, A. Cole, *Geophys. Res. Lett.* **26**, 3525 (1999).
28. Supported by grants from the NSF Geophysics program, NASA's Solid Earth and Natural Hazards program, and the U.S. Geological Survey (USGS) National Earthquake Hazards Reduction Program. Seismic and geodetic data are archived at the Northern California Earthquake Data Center (NCEDC). F. Waldhauser kindly shared his relocated earthquake catalog shown in Fig. 2A and W. Prescott generously provided USGS GPS data. Berkeley Seismological Laboratory contribution 00-06.

28 April 2000; accepted 22 June 2000

Remobilization in the Cratonic Lithosphere Recorded in Polycrystalline Diamond

D. E. Jacob,[1]* K. S. Viljoen,[2] N. Grassineau,[3] E. Jagoutz[4]

Polycrystalline diamonds (framesites) from the Venetia kimberlite in South Africa contain silicate minerals whose isotopic and trace element characteristics document remobilization of older carbon and silicate components to form the framesites shortly before kimberlite eruption. Chemical variations within the garnets correlate with carbon isotopes in the diamonds, indicating contemporaneous formation. Trace element, radiogenic, and stable isotope variations can be explained by the interaction of eclogites with a carbonatitic melt, derived by remobilization of material that had been stored for a considerable time in the lithosphere. These results indicate more recent formation of diamonds from older materials within the cratonic lithosphere.

Cratons—the nuclei of continents—preserve relicts of Earth's oldest geologic record. The occurrence of diamonds in samples from Earth's mantle is restricted to cratonic areas (*1*), and radiogenic isotope studies of their inclusions revealed similarly old ages [3.4 to 3.6 billion years ago (Ga)] for diamond genesis in the cratonic lithosphere (*2*, *3*). Recently, however, geochemical evidence indicates the formation of diamond earlier than 1 Ga (*4*), and seismic tomography has indicated that cratonic roots have variable depths (*5*), suggesting that cratonic lithosphere is more dynamic.

Aggregates of polycrystalline diamond (framesites) (*6*) from kimberlites often contain interstitial silicates and/or sulfides of lherzolitic or eclogitic paragenesis. Both these parageneses are known from xenoliths in kimberlites and inclusions in diamonds (*7*). The small grain size of the diamonds is consistent with rapid crystallization, and the intimate intergrowth of silicates and diamond indicates contemporaneous crystallization. Framesites occur in several kimberlite pipes in southern Africa (e.g., Venetia, Premier, Jwaneng, and Orapa) and can make up several percent of the total diamond concentration in a mine.

We focused on framesites containing silicates of eclogitic affinity from the Venetia kimberlite pipe situated in the Limpopo central belt in northeastern South Africa (*8*). All samples chosen for this study contain 10 to 25 weight % (wt %) (≈0.9 to 1.4 g) eclogitic garnet, but none contain clinopyroxene. One sample (V948) contains about 1% sulfide. Eclogitic garnets from framesites have more restricted Ca contents that are generally lower than those of garnets from eclogitic xenoliths and eclogitic inclusions in diamond (*9*). However, elevated Cr_2O_3 contents, which would be expected for websteritic garnets, are not present. Mg numbers (*10*) of eclogitic garnets in framesites (Table 1) are mostly higher at lower TiO_2 concentrations than those of diamond inclusions and eclogite xenoliths. Additionally, a trend of increasing Mg number with increasing TiO_2 content is apparent, which is not reported for eclogite xenoliths and inclusions in diamond, nor is it readily explained by common rock-forming processes such as fractional crystallization. We chose samples representative of this trend and large enough to be able to carry out a complete study of major and trace elements, Rb-Sr, Nd-Sm isotopes, and oxygen isotopes on mineral separates, as well as of carbon isotopes on the diamonds.

On an isochron plot of $^{147}Sm/^{144}Nd$ versus $^{143}Nd/^{144}Nd$, the garnets fall on a straight line that, if interpreted as an isochron, yields an apparent age of 125 million years ago (Ma). The Venetia kimberlite itself, however, is 533 Ma (*8*), indicating that this line results from a mixing relation. In fact, the initial Nd isotopic ratios (measured $^{143}Nd/^{144}Nd$ ratios recalculated to the age of the kimberlite) also correlate with most other chemical parameters of the framesites, such as Mg numbers, $\delta^{18}O$ values, and ratios of trace elements in the garnets, further supporting mixing. Furthermore, stable isotope measurements display correlations between chemical parameters of the garnets (e.g., Mg number and $\delta^{18}O$) and the carbon isotopic composition of the diamond crystals (Fig. 1). Systematic relations between host diamonds and their inclusions are virtually unknown for macrocrystalline diamonds (*11*) but are reported for framesites from Orapa (Botswana) (*12*) (Fig. 1), implying that mixing could be a general process in framesite genesis worldwide.

In contrast to garnets from most eclogite xenoliths, all framesite garnets have $\varepsilon_{Nd(i)}$ values between −15.9 and −21.7 (Fig. 2). The correlation between $^{87}Sr/^{86}Sr$ and $^{143}Nd/^{144}Nd$ ratios, the mixing line, points to an end-member with even more unradiogenic Sr and Nd isotopic values. The unradiogenic Nd isotopes require an old, long-term light rare earth element (LREE)–enriched component, reminiscent of that identified in harzburgitic subcalcic garnets included in diamond (*13*). However, Sm/Nd ratios of the framesitic garnets are too high to account for the unradiogenic $^{143}Nd/^{144}Nd$ ratios and show that the isotopic signature must be inherited.

All four garnets show similar trace element patterns with high heavy rare earth element (HREE) and low LREE contents that are typical for garnets (Fig. 3A). However, trace element zonation detected by in situ trace element measurements in one of the samples (V948) shows that framesite formation may have occurred shortly before kimberlite eruption. Figure 3B shows zones detected by time-resolved laser ablation inductively coupled plasma mass spectrometry (ICP-MS) (LAM) analysis in sample V948 that are enriched in many incompatible elements and LREE. In these zones, which cannot be attributed to cores or rims, Sr contents are enriched by up to a factor of 19 and are accompanied by an enrichment in LREE, similar to features of

[1]Institut für Geologische Wissenschaften, Universität Greifswald, F.-L. Jahnstrasse 17a, D-17487 Greifswald, Germany. [2]DeBeers Geoscience Center, Post Office Box 82232, Southdale 2135, South Africa. [3]Department of Geology, Royal Holloway University of London, Egham, Surrey TW20 0EX, UK. [4]Max-Planck Institut für Chemie, Saarstrasse 23, D-55122 Mainz, Germany.

*To whom correspondence should be addressed.